frontiers | Frontiers in Soft Matter

TYPE Original Research
PUBLISHED 06 March 2024
DOI 10.3389/frsfm.2024.1354122

OPEN ACCESS

EDITED BY
Kay Saalwächter,
Martin-Luther-University Halle-Wittenberg, Germany

REVIEWED BY
Michael Gradzielski,
Technische Universität Berlin, Germany
Thomas Hellweg,
Universität Bielefeld, Germany

*CORRESPONDENCE
Marcelo G. de Oliveira,
mgo@unicamp.br
Tomás S. Plivelic,
tomas.plivelic@maxiv.lu.se

RECEIVED 11 December 2023
ACCEPTED 14 February 2024
PUBLISHED 06 March 2024

CITATION
Bomediano MP, da Silva LCE, Mota-Santiago P, de Oliveira MG and Plivelic TS (2024), Monitoring the micellar packing of photo-crosslinkable Pluronic F127 dimethacrylate during 3D printing.
Front. Soft Matter 4:1354122.
doi: 10.3389/frsfm.2024.1354122

Monitoring the micellar packing of photo-crosslinkable Pluronic F127 dimethacrylate during 3D printing

Mateus P. Bomediano[1], Laura C. E. da Silva[1], Pablo Mota-Santiago[2], Marcelo G. de Oliveira[1]* and Tomás S. Plivelic[2]*

[1]Instituto de Química, Universidade Estadual de Campinas (UNICAMP), Campinas, Brazil, [2]MAX IV Laboratory, Lund University, Lund, Sweden

Pluronic F127 dimethacrylate (F127-DM) inks exhibit potential for 3D printing biomaterials due to their combined gelation and photo-crosslinking capabilities. Previous studies have explored their application in extrusion 3D printing of medical devices, relying on their long-range micellar ordering to impart mechanical stability, stretchability, and control over drug delivery. However, there is a lack of information regarding the impact of the extrusion and photo-crosslinking processes on the micellar ordering of F127-DM. Herein, we employed *in operando* 3D printing synchrotron small-angle X-ray scattering (SAXS) to analyze the influence of various printing parameters, including nozzle shape, nozzle size, extrusion rate, ink composition, and photo-crosslinking, on the micellar ordering of F127-DM. Our findings from 2D SAXS patterns indicate orientation of the micellar packing clusters along the flow direction. The nozzle diameter and shape emerged as crucial parameters, leading to increased disruption of long-range ordering. Furthermore, 1D SAXS curves during UV-Vis light exposure and photo-crosslinking revealed a partial preservation of the micellar packing structure, with cluster size reduction, and coexisting with randomly distributed micelles and unimers. These results underscore the importance of *in operando* synchrotron experiments for the systematic study of 3D printing parameters from a nanostructure perspective.

KEYWORDS

***in operando* 3D printing, time-resolved SAXS, Pluronic, micellar inks, hydrogels, photo-crosslinking, micellar packing**

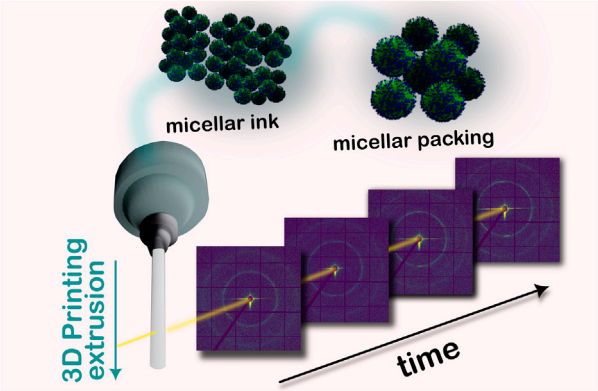

GRAPHICAL ABSTRACT

1 Introduction

Pluronic is the trade name of a class of non-ionic triblock copolymers comprised of poly(ethylene oxide)-poly(propylene oxide)-poly(ethylene oxide) (PEO-PPO-PEO). Among the various types of Pluronics, designated by different acronyms according to their hydrophilic-lipophilic balance (HLB) and relative size of the PPO block, Pluronic F127 (PEO_{99}–PPO_{65}–PEO_{99}) (F127), is one of the most widely used in biomedical applications due to its low toxicity and good biocompatibility (Zarrintaj et al., 2020). Pluronics undergo spontaneous micellization and gelation processes in aqueous solution, induced by increasing the concentration of the polymer solution or the temperature (Wanka et al., 1994). Pluronics where the PEO block is much longer than the PPO block, such as F127, form spherical micelles and are characterized by a gelation process resulting from the micelles being packed into lattices that might have a face-centered cubic (fcc) or body-centered cubic (bcc) unit cell. At high concentrations lamellar or hexagonal phases can also be present (Mortensen and Pedersen, 1993; Wanka et al., 1994). The amphiphilic properties of PEO-PPO-PEO micelles have facilitated the advancement of various Pluronic hydrogels for drug delivery in biomedical applications (Yu et al., 2021). More recently, Pluronic hydrogels are being increasingly explored for use in 3D extrusion printing, due to their reversible thermal gelation properties (Gioffredi et al., 2016).

The emergence of 3D printing in biomedical applications has rapidly enabled the employment of hydrogels as ink matrices due to their mechanical and rheological properties, such as the shear-thinning behavior that allows extrudability (Song et al., 2010; Highley et al., 2015). The extrusion-based 3D printing is the most widely used technique due to its low machinery requirements and accessibility. The 3D printing of hydrogels, also referred in literature as semi-solid extrusion (Seoane-Viaño et al., 2021), involves adding the material, either the hydrogel precursors or the hydrogel itself, inside a syringe, which is coupled with the printer head motor to extrude continuous filament through a nozzle. The filament is then deposited onto the print plate, in a layer-by-layer manner, based on a 3D computer model. Pneumatic mechanisms, pistons, or screws can be employed to drive the extrusion of the ink through the nozzle (Abu Owida, 2022). Post-extrusion treatments such as light exposure, annealing, or solvent treatment can offer a pathway to trigger physical or chemical crosslinking mechanisms that retain the shape fidelity of the hydrogel-based constructs after printing (GhavamiNejad et al., 2020; Puza and Lienkamp, 2022). Semi-solid extrusion has potential for fabricating biomedical devices such as scaffolds and implants for tissue engineering (Bashiri et al., 2023).

Although native thermoreversible Pluronic hydrogels can be used for the 3D printing of constructs by extrusion, they have poor stability and fall apart if manipulated. In addition, Pluronic molecules are water soluble, and the constructs dissolve if exposed to aqueous environments (Akash and Rehman, 2015; Gioffredi et al., 2016). To overcome these limitations and expand the potential medical/pharmaceutical uses of Pluronic hydrogels, various chemical crosslinking strategies have been described to preserve the integrity of the constructs in different environmental conditions (Niu et al., 2009). Substitution of the hydroxyl groups with photoreactive groups (e.g., acrylate or methacrylate) is the most common strategy to allow the formation of chemical crosslinks between molecules that keep the micellar packing geometry after extrusion. Several reports have explored the use of Pluronics with terminal photoreactive groups for semi-solid extrusion 3D printing, assuming that the micellar packing is preserved after printing and photo-crosslinking (Müller et al., 2015; Smith et al., 2018). Although the printability of photo-crosslinkable Pluronics is well-known, the impact of the shear stress and photo-crosslinking on the long-range ordering of the micellar packing is unclear. A systematic understanding of these phenomena becomes important not only from the point of view of fundamental knowledge, but also from the point of view of how micellar packing in Pluronics could affect other interesting properties, such as drug diffusion.

Preliminary studies by Shriky et al. (2020) aimed to simulate real-body injection flow systems subjected to shear stress using small angle X-ray scattering (SAXS) measurements, and showed the presence of Bragg peaks associated with the cubic phases of F127 hydrogels. During extrusion, using a 3 mm-diameter channel as an *in situ* injection flow system, these authors reported a shift in the position of the Bragg peaks, suggesting the loosening of the packed structure and the transition to a less ordered state (Shriky et al., 2020). The first investigation involving extrusion-

based 3D printing of native Pluronics was reported by Rodriguez-Palomo et al., who used SAXS measurements to evaluate the shear-induced anisotropy in Pluronic-based inks that were arranged in hexagonal and lamellar phases. In this study, the disturbance of the micellar organization was evidenced by the broadening and disappearance of the Bragg diffraction peaks in the SAXS patterns (Rodriguez-Palomo et al., 2021).

In addition, several studies have reported the use of rheology associated with SAXS (rheology-SAXS) and small-angle neutron scattering (rheology-SANS) to characterize the effect of shear on the structure of colloidal liquid crystals (Bates et al., 1994; Mcconnell et al., 1995; Mortensen et al., 1995; Mortensen, 2004; Pozzo and Walker, 2007). While these studies offer valuable insights into interpreting the numerous reversible structural changes that may occur during the shear of micellar inks, it is important to note that the geometry of the sample environments in rheology experiments significantly differs from those employed in extrusion 3D printing. This disparity poses a challenge in establishing a direct correlation with the extrusion process.

In this work, we present results from *in operando* 3D printing synchrotron SAXS measurements used to monitor the temporal evolution of the micellar packing of Pluronic F127 dimethacrylate (F127-DM) hydrogel filaments extruded under different conditions, including extrusion rates, nozzle diameter and geometry, and ink compositions with different methacrylation degrees. The experiments were carried out using a unique, custom-built extrusion-based 3D printer, tailored for *in operando* analysis. The monitoring of the structural changes in F127-DM inks induced by the photo-crosslinking process was performed both under static conditions and immediately after extrusion. The results we gathered provide fundamental insights on how the printing parameters may affect the micellar packing of photo-crosslinked F127-DM hydrogels.

2 Materials and methods

2.1 Materials

Pluronic F127 (PEO_{99}–PPO_{65}–PEO_{99}; Mn 12600 g mol^{-1}), methacrylic anhydride (MA), and lithium phenyl-2,4,6-trimethylbenzoylphosphinate (LAP) were obtained from Sigma-Aldrich. All reagents were used without further purification. Ultrapure Milli-Q water (resistivity 18.2 MΩ cm) was used in all procedures.

2.2 Pluronic dimethacrylate (F127-DM) synthesis

The terminal hydroxyl groups of F127 were subjected to a methacrylation reaction with methacrylic anhydride to produce F127-DM using a microwave-assisted methodology based on the study described by Lin-Gibson et al., 2004. Herein we used 1:1 and 5:1 methacrylic anhydride to Pluronic molar ratios to obtain F127-DM with two different methacrylation degrees: 54% and 95%, respectively. These F127-DMs are referred to hereafter as the F127-DM50 and F127-DM100, respectively. Characterization of the F127-DM by ^{1}H-NMR allowed identifying the signal of the vinyl protons of the methacrylate group (=CH_2) at δ = 5.69 ppm and δ = 6.03 ppm, and the signals of the three protons of the methyl substituent (=CCH_3) at δ = 1.88 ppm (Supplementary Figure S1). The methacrylation degree was calculated from the integrated area of the specific ^{1}H-NMR signal assigned to the protons of the terminal methacrylate group, according to the method proposed by Lin-Gibson et al.

2.3 Preparation of F127-DM and F127 solutions

Aqueous solutions of 30 wt% native F127 and F127-DM were prepared by the cold method, slowly adding the polymer, in the form of flakes, to deionized water under magnetic stirring in an ice bath. For the 3D printing measurements, the solution was poured into a syringe coupled with a lid and left overnight in a refrigerator (8°C) for the removal of air bubbles prior to use. For the experiments that required photo-crosslinking, 0.5 wt% of the LAP photoinitiator was added to the solutions prior to pouring into the syringe. All syringes were stored in a refrigerator (8°C), protected from ambient light.

2.4 In operando 3D printing small angle X-ray scattering (SAXS) measurements

The *in operando* small angle X-ray scattering (SAXS) measurements were performed in a custom-built 3D extrusion-based printer (3DBS - 3D Biotechnology Solutions) at the CATERETÊ beamline at the Sirius Synchrotron Laboratory (LNLS/CNPEM, Campinas, SP Brazil). A photograph of the experimental setup is shown in Figure 1A. A wavelength λ = 0.1378 nm and a sample-to-detector distance of 1.715 m were used on the experiments, resulting in a q-range of 0.0415—3.4182 nm^{-1} (where $q = \frac{4\pi}{\lambda} sin\,\theta$, and 2θ is the scattering angle). The q-range calibration was performed using the standard silver behenate. The 2D SAXS images were collected with a PiMEGA detector (55 × 55 μm^2 pixel size and 3072 × 3072 pixel-array, PITEC).

Preliminary experiments were performed at the CoSAXS beamline at the MAXIV Laboratory (Lund, Sweden) to determine the most relevant extrusion parameters. We selected cylindrical nozzles with internal diameters of 1 mm and 0.4 mm, and a conical nozzle with an internal outlet diameter of 0.4 mm for the experiments carried out at CATERETÊ beamline (Meneau et al., 2021). We also studied three different extrusion rates: 1, 3, and 10 mm min^{-1}. The shear rates estimated for each extrusion rate are shown in Supplementary Figure S2 for the cylindrical nozzles. In both beamlines, the remote control of the device was performed with the free software Pronterface©.

The *in operando* measurements were conducted at 30°C (at the 3D printer hot-end). In total, 48 frames were acquired in one position of the filament, as shown in Figure 1B, with an exposure time of 5 s per frame and a 0.1 s delay time between them (4 min total exposure to prevent radiation damage), which comprised both the extrusion process and the nanostructural recovery of the hanging filament.

For the 1 mm F127-DM filament, additional 3 min of visible light exposure was performed when needed (source LMI-6000 LED Illuminator from Dolan Jenner Fiber-Lite, 780 lumens power).

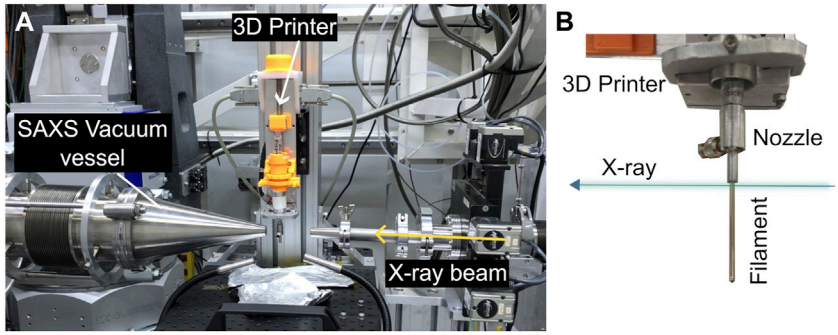

FIGURE 1
(A) Experimental setup for the *in operando* 3D printing measurements at the CATERETÊ beamline. **(B)** Photograph of the hanging filament showing the X-ray beam direction and incident position.

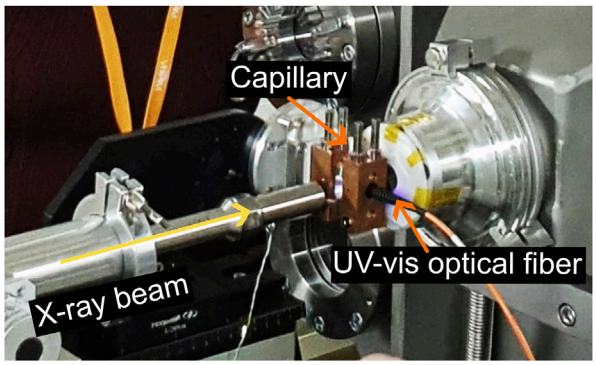

FIGURE 2
Experimental set-up for the *in situ* photo-crosslinking measurements performed at the CoSAXS synchrotron beamline at the MAX IV Laboratory.

Afterwards, the filament was measured with one single X-ray exposure of 20 s.

2.5 *In situ* photo-crosslinking SAXS experiments

In situ photo-crosslinking experiments were performed at the CoSAXS beamline at MAXIV Laboratory (Lund, Sweden) (Plivelic et al., 2019) using the experimental setup shown in Figure 2. The inks containing the LAP photoinitiator were placed in 1.5 mm diameter quartz capillaries and thermalized at room temperature before the experiments. The UV-Vis irradiation was performed perpendicularly to the X-ray propagation direction using an LED light source with maximum emission at 405 nm coupled to a 400 µm-diameter fiber optic (M405FP1 Thorlabs, 24.3 mW nominal power at the output of the fiber). Irradiation with λ = 0.0999 nm at a sample-to-detector distance of 3.471 m was used in all experiments, covering the q-range $0.0391 \leq q \leq 2.6493$ nm^{-1}. 2D scattering patterns were collected using a Eiger2 4 M detector (Dectris, 75 × 75 mm^2 pixel size and 2068 × 2162 pixel-array). SAXS data were collected during *in situ* UV-Vis irradiation in

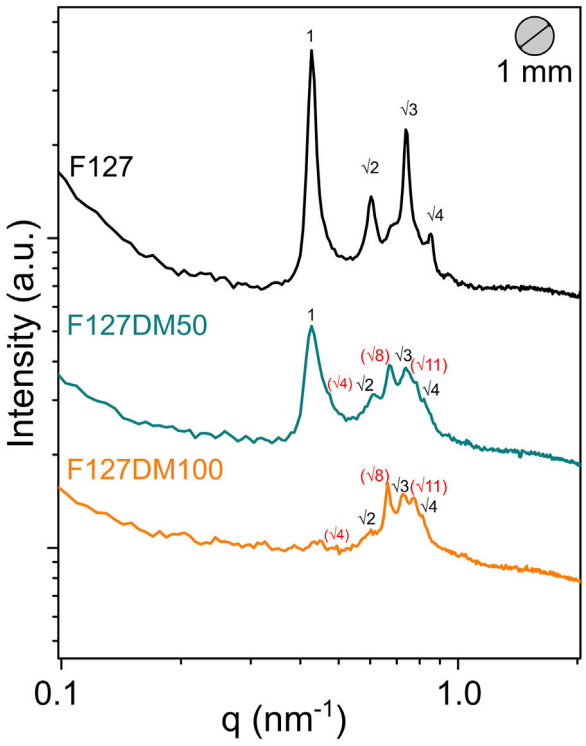

FIGURE 3
Representative SAXS curves of the F127, F127-DM50, and F127-DM100 inks using a 1 mm cylindrical nozzle and 3 mm min^{-1} extrusion rate. The patterns shown are an average of the last five frames acquired during *in operando* extrusion-recovery experiments. The data is shifted vertically for clarity.

35 frames with an exposure time of 0.2 s per frame (7 s total exposure) using a vertical scan collection mode to acquire each frame at a fresh spot.

2.6 SAXS data analysis

The radial integrations of the *in operando* and *in situ* SAXS data were performed at the respective beamlines using an in-house

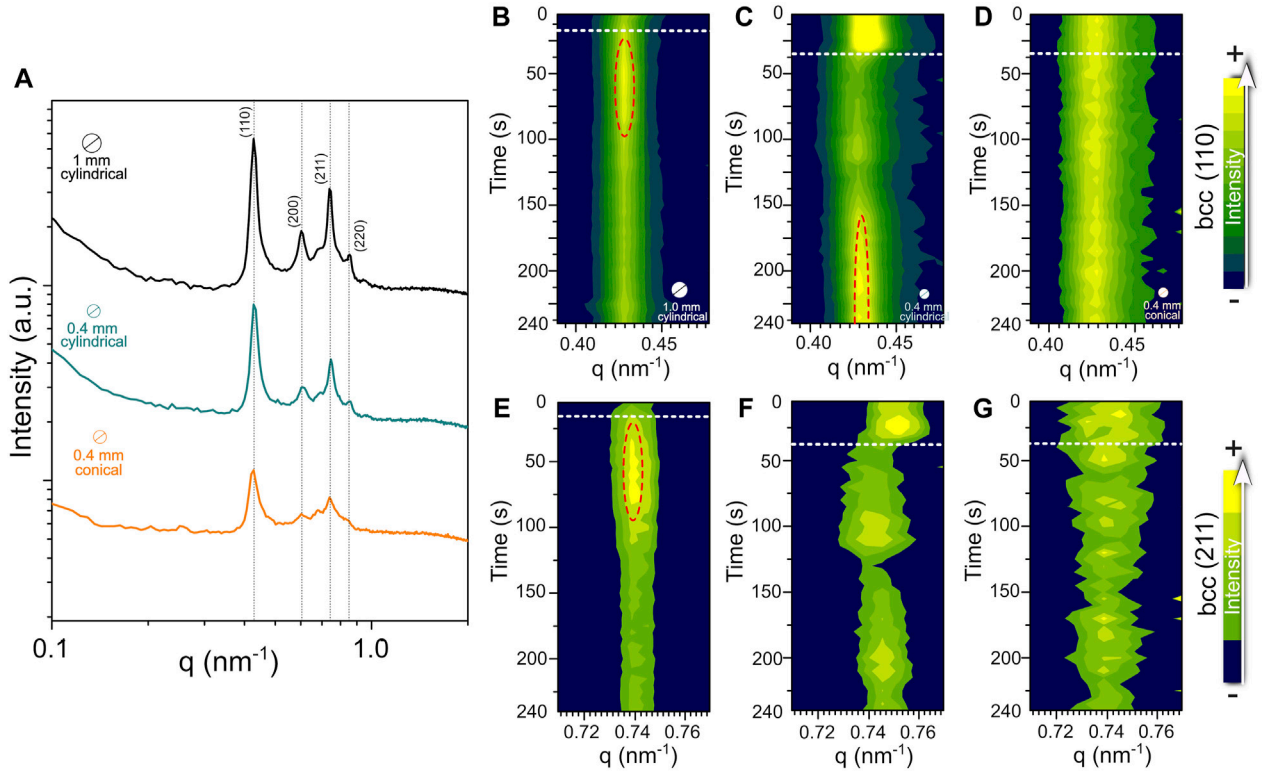

FIGURE 4
(A) Representative 1D SAXS patterns for F127 filaments obtained with a 3 mm min^{-1} extrusion rate using a 1 mm cylindrical, a 0.4 mm cylindrical and a 0.4 mm conical nozzles. The curves are an average of the last five frames acquired on each experiment, normalized by filament thickness. Contour plots showing the intensity evolution of the (110) bcc plane during *in operando* extrusion-recovery experiments using **(B)** 1 mm cylindrical, **(C)** 0.4 mm cylindrical, and **(D)** 0.4 mm conical nozzles. Contour plots showing the intensity evolution of the (211) bcc plane using **(E)** 1 mm cylindrical, **(F)** 0.4 mm cylindrical, and **(G)** 0.4 mm conical nozzles. Intensity color scales are unique for each sample and plane. White dashed lines represent the end of the extrusion process (i.e., material ejection through the nozzle) and the beginning of the micelle packing recovery. Areas surrounded by the dashed red lines in Figures 4B, C, E highlight the time intervals in which the intensity of the peaks associated with the (110) and (211) bcc planes achieved the highest intensities.

developed software. Structure determination was performed according to (Jang et al., 2013) and by comparing peak ratios. Subsequently, the cell parameter (a) was determined by the linear fitting of the $d_{hkl} = (\frac{2\pi}{q})$ vs. $\frac{1}{\sqrt{h^2+k^2+l^2}}$ plot, where h, k, and l are the Miller indices of the cubic phase and a is the slope (Wu et al., 1998). Linear fittings and contour plots were obtained using the software Origin 8.5®.

The azimuthal intensity patterns, I(φ), were obtained by azimuthal integration of the 2D SAXS patterns, using the Fit2D: Detector Calibration/Correction software (V17.006) using a q-range of 0.403–0.444 nm^{-1} from the azimuthal angle φ = 0 to φ = 360°.

3 Results

3.1 Ink composition

Figure 3 shows representative SAXS patterns of the extruded filaments obtained from the F127 (dark curve), F127-DM50 (green curve), and F127-DM100 (orange curve) hydrogels using a 1 mm cylindrical nozzle and an extrusion rate of 3 mm min^{-1}. The prominent Bragg peaks shown for the native F127 correspond to a sharp first diffraction peak (with maximum at $q^* = 0.427$ nm^{-1}), followed by less intense peaks at q-value ratios, q/q^*, of 1: √2: √3: √4, which correspond to a body-centered cubic (bcc) micellar packing (Jang et al., 2013), leading to a unit cell parameter of a = 20.7 nm. The Miller indices for these peaks are: (110), (200), (211) and (220), respectively.

The Bragg peaks associated with the bcc structure were also identified in the SAXS patterns of the F127-DM50 and F127-DM100 hydrogels, although in much lower intensities and less defined profiles. Furthermore, the diffraction pattern for both F127-DM filaments also showed distinctive Bragg peaks that could not be associated with the bcc structure. These peaks appear at q-value ratios of √4: √8: √11, suggesting the coexistence of a face-centered cubic (fcc) micellar packing. The Miller indices for these peaks are: (200), (220) and (311), respectively (Wu et al., 1998). Here, the first order fcc peak (√3) assigned to the Miller index (111) is possibly overlapped with the q* peak of the bcc phase. The coexistence of the bcc and fcc structures in Pluronic-based materials has been extensively reported in the literature (Mortensen et al., 2008).

The main changes in the SAXS patterns when comparing the native F127 hydrogel with the F127-DM50 and F127-DM100

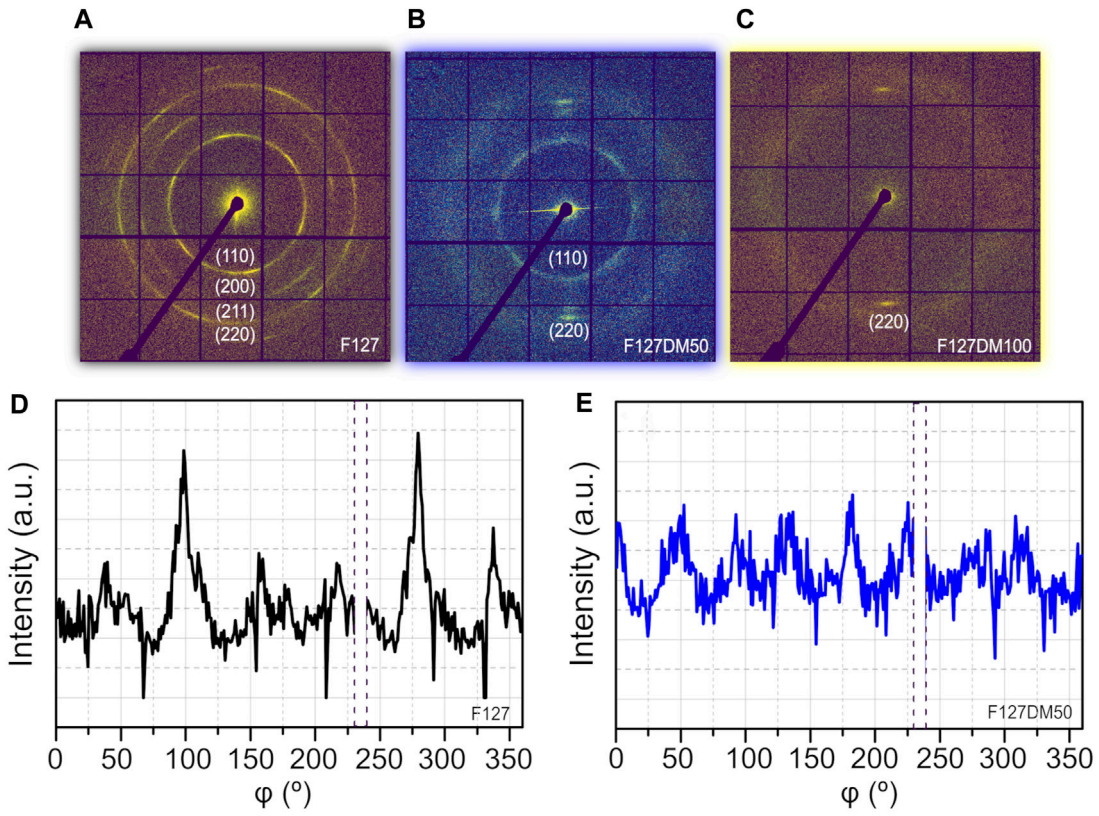

FIGURE 5
Representative 2S SAXS patterns collected with a 1 mm nozzle at a 3 mm min^{-1} extrusion rate for **(A)** F127, **(B)** F127-DM50, and **(C)** F127-DM100 filaments. Azimuthal scattering intensity integration for **(D)** F127 and **(E)** F127-DM50 filaments at the (110) bcc reflection.

hydrogels in Figure 3 are the broadening of the peak associated with the (110) bcc plane of the F127-DM50 hydrogel and its complete disappearance in the F127-DM100 hydrogel. Additionally, the peak associated with the (111) fcc plane is absent in the SAXS patterns of the F127-DM50 and F127-DM100 hydrogels. Supplementary Figure S3 shows the SAXS patterns of F127, F127-DM50 and F127-DM100 obtained 4 min after the filaments exited the 1 mm nozzle tip at an extrusion rate of 3 mm min^{-1} and approximately 20 min after the end of extrusion. It can be seen that the peak associated with the (110) bcc plane reappears after extrusion, indicating a nanostructural recovery. A similar result has been reported for *in situ* rheological small-angle scattering (rheo-SAS) experiments of Pluronics, and has been attributed to slip mechanisms, which involve the movement of micellar planes when an external shear stress is applied (Ackerson and Clark, 1984; Pozzo and Walker, 2007). The moving crystallographic planes are often the ones with the largest interplanar distances and serve as preferred pathways for dislocations. For the bcc structure, the (110) plane has the largest interplanar distance and is considered to slide preferentially in the <111> direction. For the fcc structure, the (111) plane slides preferentially in the <110> direction (Mortensen, 2004). Therefore, it is reasonable to assume that the F127-DM inks absorb the plastic deformation imposed by the flow through the sliding of the (110) bcc plane in the <111> direction and the (111) fcc plane in the <110> direction.

In summary, the native F127 filament showed a pure bcc phase, while the F127-DM50 and the F127-DM100 filaments showed a combination of bcc and fcc structures. For both phases, the reflection plane associated with the first diffraction peak was susceptible to slip mechanisms.

3.2 Impact of nozzle size and shape

Figure 4A shows representative SAXS patterns obtained for the native F127 filaments at the end of the extrusion-recovery measurement performed using a constant 3 mm min^{-1} extrusion rate and three different nozzle shapes: 1 mm cylindrical, 0.4 mm cylindrical, and 0.4 mm conical. The characteristic Bragg peaks associated with the bcc phase were found for all cases.

For the 1 mm nozzle, well-defined high intensity peaks were found, while for the 0.4 mm cylindrical nozzle, the peaks are broader (i.e., larger full-width at half maximum, FWHM) and the intensity is reduced. This effect is even more pronounced when using the conical nozzle (Figure 4A). A similar behavior was found for the F127-DM50 (Supplementary Figure S4) and the F127-DM100 (Supplementary Figure S5), for both the bcc and the fcc phases. The fcc phase also showed evidence of structural disruption due to the absence of the (111) fcc slip plane (Supplementary Figure S5). These changes in the SAXS patterns can be attributed to a reduction of the micellar long-range ordering.

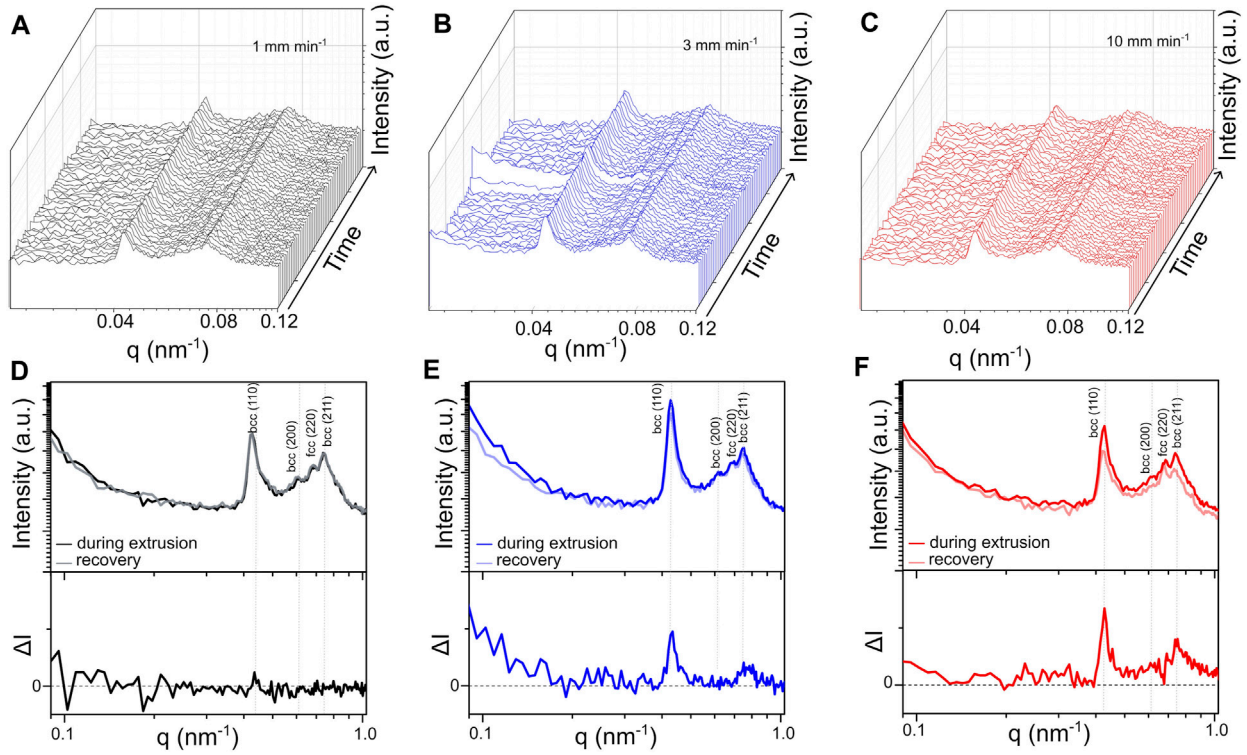

FIGURE 6
Time evolution of the SAXS curves during 3D printing and nanostructural recovery of F127-DM50 extruded through a 0.4 mm cylindrical nozzle at **(A)** 1 mm min^{-1}, **(B)** 3 mm min^{-1} and **(C)** 10 mm min^{-1}. Representative SAXS patterns obtained during extrusion (dark curves) from a 0.4 mm cylindrical nozzle at **(D)** 1 mm min^{-1}, **(E)** 3 mm min^{-1} and **(F)** 10 mm min^{-1}; the representative SAXS patterns obtained during nanostructural recovery (light curves); and the scattering intensity difference between extrusion and recovery (ΔI). The patterns shown in **(D–F)** are an average of five consecutive frames.

The contour plots associated with the evolution of the (110) and the (211) bcc peaks during the extrusion-recovery process are shown in Figures 4B–G, respectively. The white dashed horizontal lines mark the end of the extrusion process, when the filament ejection is finished. This occurs at a specific time for each nozzle diameter.

During filament ejection, the Bragg peaks associated with the (110) and the (211) bcc planes shift to lower q-values, which is attributed to a reduction of the unit cell parameter (Supplementary Figure S6), as an effect of shearing. The (211) bcc plane slipping in the <111> direction is also part of the possible plane dislocations described by Mortensen (2004). However, this fact was not observed for the 0.4 mm conical nozzle (Figures 4D, G), as a consequence of the reduced long-range ordering.

During the elapsed time from the end of filament ejection (white dashed line) to the end of the experiment (bottom of the plots), the (110) and the (211) bcc planes showed an intensity increase (40–90 s for the 1 mm nozzle; 150—240 s for the 0.4 cylindrical nozzle), that is gradually reduced afterwards. After the material injection ceased, the nanostructural loss still proceeds due to the cooperative movement of the polymer chains (see 40—125 s, Figure 4C). Once the shear tensions are ceased and the chain extension is at its maximum, entropy becomes the driving force for the opposite cooperative movement towards nanostructural recovery (Mortensen, 2004; Pozzo and Walker, 2007). These results suggest that the bcc phase structure is partially recovered, at different timescales for each nozzle, after the slip plane dislocations.

If a laminar flow is assumed for all the printing conditions and ink compositions, which is reasonable since printability was reached in all cases, then a shear force gradient occurs in a cylindrical nozzle, where the center of the flow has a lower shear stress than the edges (Jiang et al., 2020). For a constant volume flow per min, when a wider nozzle is used, such as the 1 mm, the shear gradient is less pronounced, and the micellar packing is less disturbed. This is also the reason for the more rapid nanostructural recovery with the 1 mm than the 0.4 mm nozzle.

Interestingly, both the bcc and the fcc arrangements were significantly more disturbed when the conical nozzle was used. Additionally, q-shift to lower values was clearly observed for the (220) and the (311) fcc peaks, with no structural recovery during the timeframe of the experiment. *A priori* this was not expected, since literature reports mention that the gradual diameter variation of the conical nozzle leads to a smoother pressure gradient, which reduces the shear stress during the 3D printing of bioinks (Bom et al., 2022).

Another important effect of the shear stress is structural anisotropy, which is evidenced at the 2D SAXS patterns as scattering intensity changes as function of the azimuthal angle for each scattering vector q. Figure 5 shows the 2D scattering images collected at 240 s of experiment for native F127 (Figure 5A), F127-DM50 (Figure 5B), and F127-DM100 (Figure 5C) filaments after extrusion through a 1 mm nozzle at 3 mm min^{-1}. Discrete intensity regions (instead of continuous rings) indicate the existence of

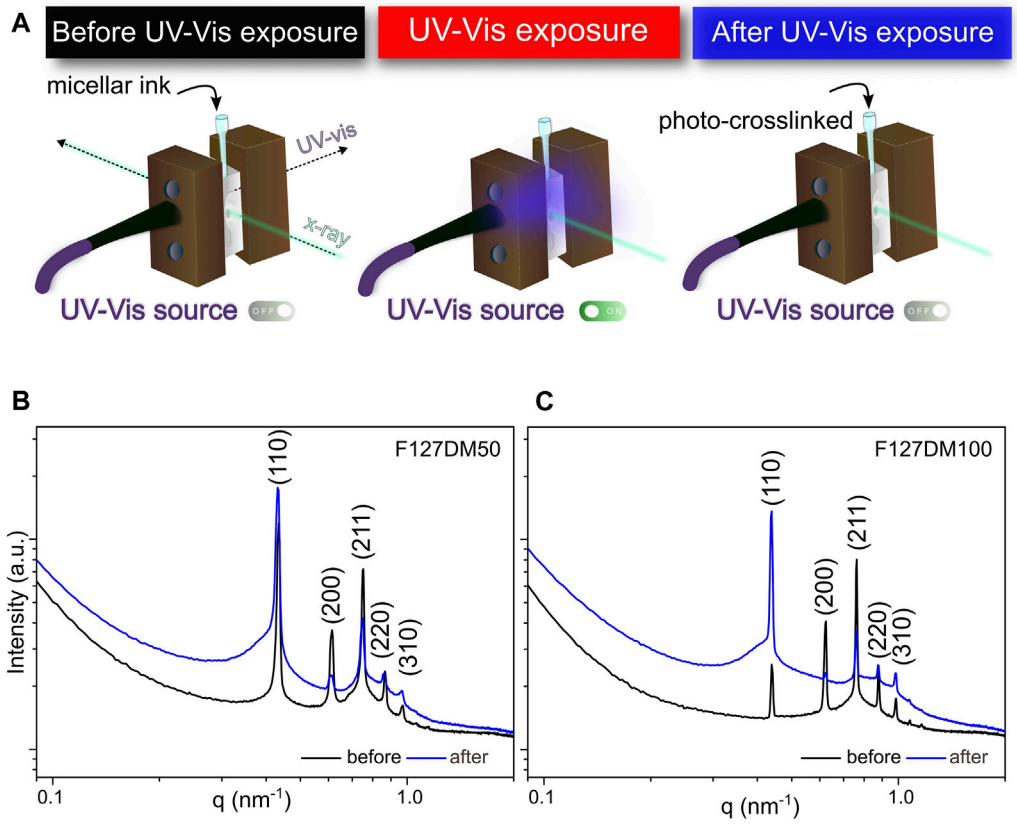

FIGURE 7
(A) Schematic illustration of the *in situ* UV-Vis photo-crosslinking/SAXS experiment. **(B)** F127-DM50 and **(C)** F127-DM100 SAXS patterns before and after photo-crosslinking.

preferential orientation on the system. Figure 5D shows the azimuthal intensity dependence for the (110) bcc peak. A sixfold scattering, translated into 6 evenly spaced high-intensity peaks (39.5°, 98.5°, 156.5°, 216.5°, 279.5°, and 337.5°), is clearly observed during the recovery time, indicating that the micellar packing in the F127 filament is anisotropic. Higher intensities are observed in the meridional direction (at 98.5° and 279.5°, Figure 4D). A similar behavior is observed for the 0.4 mm nozzles, cylindrical (Supplementary Figure S7) and conical Supplementary Figure S8). However, due to the decrease of long-range ordering, the intensity distribution along the ring is more evenly distributed.

For the F127-DM50 filament (Figure 5B), a similar behavior is observed for the bcc phase, however, with lower (110) peak intensity than the analogous F127. Figure 5E shows the corresponding azimuthal plot. The integration is in line with the sixfold anisotropic texture but exhibits a more isotropic scattering intensity distribution compared to the native F127 filament (Figure 5D). No significant differences are observed in the meridional direction.

The fcc phase, present in both F127-DM50 and F127-DM100 filaments (Figures 5B, C respectively), is also oriented with the flow direction since the scattering intensity halo associated with the (220) plane of the fcc phase is concentrated at the meridional section. The reduced anisotropy found for both the bcc and the fcc phases of the F127-DM filaments, in comparison with the F127 filament, is a confirmation that reduced long-range ordering (Figure 3) leads to more isotropic scattering intensity distribution.

In summary, our findings suggest that large bcc clusters are present for both the F127 and the F127-DM50 filaments and align under flow, in order to put the (110) bcc slip plane parallel to the flow direction (e.g., scattering preferentially at the meridional positions). The (110) plane slipping process becomes more significant with the methacrylate groups at the chain ends. As a result, the bcc cluster size is reduced, broadening the width of their associated Bragg peaks. The smaller clusters are more mobile and, during nanostructural recovery become more isotropically oriented. A similar phenomenon may also be observed for the fcc phase due to the absence of the (111) fcc slip plane. The fcc phase clusters also align under flow, having the (220) plane parallel to the flow direction. Not only composition but also the increase of shear stress (going from the 1 mm cylindrical to the 0.4 mm cylindrical and then to the 0.4 mm conical nozzle) explains the behavior of our data.

3.3 3D printing extrusion rate

Figure 6 shows the time evolution of the SAXS curves during the extrusion of F127-DM50 filaments with the 0.4 mm cylindrical nozzle at 1 mm min^{-1} (Figures 6A, D), 3 mm min^{-1} (Figures 6B, E) and 10 mm min^{-1} (Figures 6C, F) extrusion rate. At 1 mm min^{-1} extrusion rate no distinctive changes in the SAXS curves are observed, which is highlighted by the scattering intensity

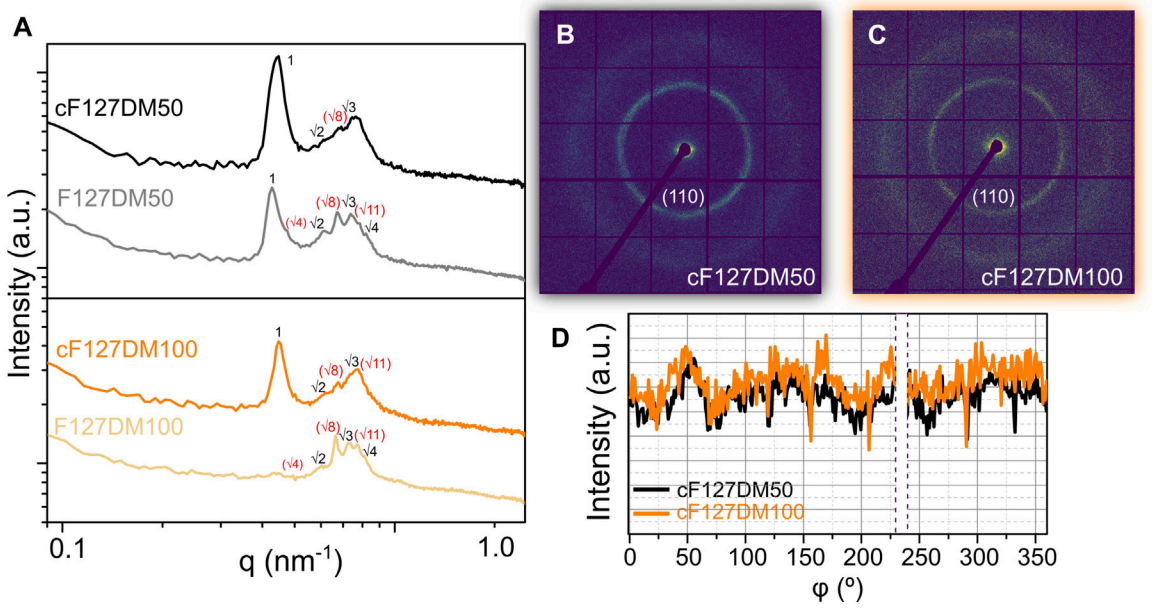

FIGURE 8
(A) Representative SAXS curves of F127-DM50 (grey) and F127-DM100 (light orange) filaments obtained with a 1 mm cylindrical nozzle and 3 mm min^{-1} extrusion rate, and their corresponding photo-crosslinked samples, cF127-DM50 (black) and cF127-DM100 (orange). 2D SAXS patterns of **(B)** cF127-DM50 and **(C)** cF127-DM100. **(D)** Azimuthal plot of the (110) bcc peaks for cF127-DM50 (black) and cF127-DM100 (orange).

difference (ΔI) between representative 1D SAXS curves of the extrusion and recovery processes being zero along the entire q-range (Figure 5D). Conversely, at higher extrusion rates a significant scattering intensity reduction is observed, particularly for the Bragg peaks associated with the bcc phase at 10 mm min^{-1} (Figure 5F). These results are most likely a consequence of the increasing shear stress imposed by the increasing printing speed. The fact that the bcc phase is preferentially disrupted may be a consequence of the lower occupancy of the bcc cell unit respective to the closely packed fcc cell unit (Eiser, et al., 2000). Furthermore, existing literature indicates that the slip mechanism in the bcc phase does not involve the smooth sliding of perfect layers over each other. Instead, it operates through intricate mechanisms that introduce greater friction (Mcconnell et al., 1995).

3.4 Photo-crosslinking

To evaluate the impact of photo-crosslinking on the nanostructure of F127-DM filaments we initially performed *in situ* UV-Vis photo-crosslinking experiments with the hydrogel samples contained in capillaries (Figure 7). Subsequently, we evaluated the combination of 3D printing and photo-crosslinking by *ex situ* photo-crosslinking post extruded filaments (Figure 8). Figure 7A illustrates the workflow of the *in situ* UV-Vis photo-crosslinking experiments. Initially, F127-DM50 and F127-DM100 inks were scanned under room temperature, with X-rays at different vertical positions to assess the gel structure prior to UV-Vis irradiation. Subsequent irradiation of the capillaries, using a fiber optic coupled to the sample holder, was carried out in parallel to a vertical scan of the capillaries for direct spatial comparison. After irradiation, another vertical scan was performed to assess the final micellar nanostructure. The SAXS curves of the hydrogels before and after irradiation are shown in Figures 7B, C, respectively. Supplementary Figure S9 shows the 3D plots of the time-resolved SAXS curves during photo-crosslinking.

After comparison of the averaged scattering intensity curves, UV-Vis exposure does not seem to cause a shift in the peak positions, whilst their intensities are significantly altered, and the base of the peaks are broadened, indicating an increase of the scattering associated with the degree of ordering of the micellar packing. These results show that the micellar packing is partially retained after the photo-crosslinking (i.e., cluster size reduction) and these ordered structures coexist with isotropically distributed micelles (Picheth et al., 2019). The noticeable sharper structures (Bragg peaks) observed for these experiments compared to previous plots are related to different beamline optimizations.

To evaluate the combined effect of 3D printing and photo-crosslinking, F127-DM50 and F127-DM100 filaments were exposed to an external visible light source for 3 min, after the 240 s recovery period after extrusion (Figure 8). The vanishing of the absorbance band at 1636 cm^{-1}, assigned to the C=C stretching vibration of the vinyl group of the terminal methacrylate moieties of F127-DM after irradiation of the extruded filament indicates a photo-crosslinking efficiency of 100%, implying the absence of residual methacrylate groups in the photo-crosslinked F127-DM hydrogel (Supplementary Figure S10).

For crosslinked F127-DM50 (cF127DM50) an increased intensity and a shift to higher q-values are observed for the (110) bcc peak (compared to F127DM50), whereas for crosslinked F127-DM100 (cF127DM100) this peak appears during photo-

crosslinking, indicating concomitant nanostructural recovery. At higher q, the structural behavior seems to be opposite, the peaks are absent or very distorted on the cross-linked hydrogels, compared to the non-crosslinked ones. Even further, the fcc phase is mostly lost, since the (200) and the (220) peaks are very reduced. Figures 8B, C show the 2D SAXS patterns for cF127DM50 and cF127DM100, while Figure 8D shows the azimuthal plot for the (110) bcc peak. In comparison with the 2D patterns in Figure 5, it is clearly observed that photo-crosslinking reduces the anisotropy of the patterns. This is most likely a consequence of the increased amount of isotropically distributed micelles in the system. However, the azimuthal plot shows that a weak fourfold scattering distribution is present, indicating that some bcc clusters are still unable to lose the orientation induced by the flow.

4 Discussion

While our research primarily focuses on the nanostructural effects of the extrusion and photo-crosslinking onto F127 and F127-DM inks during 3D printing, our final aim is to translate this knowledge for Pluronic 3D printing applications. With this perspective in mind, the presence of methacrylate groups at the chain ends of F127 is essential for achieving self-supported constructs. However, the peak broadening observed for F127-DM inks, compared to native F127 ink (Figure 3), suggests that the hydrophobic and bulky methacrylate groups at the chain ends reduce the long-range ordering of the system by reducing the average cluster size. In contrast, the micellar packing within the clusters might become more closely packed, through the formation of fcc clusters that coexists with bcc clusters. From a kinetic perspective, F127-DM50 and F127-DM100 inks also show increased susceptibility to shear-induced nanostructure disruption and slower nanostructural recovery.

The printability, shape fidelity and the resolution of 3D printed constructs are directly dependent on the nozzle geometry and diameter. Smaller nozzle diameters provide superior printing resolution since the layer thickness of the constructs are determined by the nozzle. Conversely, the use of larger diameter nozzles results in faster printing processes, without precision loss, but invariably hinders the resolution (Schwab et al., 2020). If the nanostructure retention is also considered, the best compromise is found by using larger diameter nozzles (e.g., 1 mm), which maximize micellar packing retention (Figure 4).

In terms of nozzle geometry, literature reports better extrudability of hydrogels when conical nozzles are employed (instead of cylindrical), due to the gradual pressure variation and the consequent smoother pressure gradient. Contrary to that, for Pluronic-based micellar inks, the conical nozzle showed the worst extrudability, with low precision and high nanostructural disruption.

To achieve scalability, reducing 3D printing times is critical. One variable that can be adjusted to achieve this objective without modifying nozzle shape and size is the extrusion rate, that is associated with the printing speed. In our experiments, we only evaluated the extrusion rate by considering the *z*-axis that is parallel to the flow direction. We verified that the higher the extrusion rate the higher the shear stress, which disrupts preferentially the bcc phase (Figure 6).

Depending on general 3D printer settings, the UV-Vis light exposure to induce photo-crosslinking can be performed simultaneously with 3D printing or as a post-processing step. We evaluated the photo-crosslinking effect on inks that were not subjected to shear stress, in capillaries (Figure 7), or shortly after printing (Figure 8A). The sharper Bragg peaks observed for the first case suggest that extensive relaxation times may lead to larger bcc clusters. However, the competitive drying of the filament during printing can affect the shape retention of the construct, being responsible for dimensional changes as well as loss of mechanical properties. From a practical perspective, drying limits the fabrication of large-scale structures, which could be overcome by controlling the humidity on the printing plate. It is worth mentioning that a time constraint, such as the 4-min recovery period we determined, is necessary to prevent water evaporation and the resulting phase transitions such as PEO block crystallization (Rodriguez-Palomo et al., 2021). Therefore, it is not feasible to reach full nanostructural recovery on the filament after printing, particularly for the F127-DM inks. On the other hand, the influence of the resting period of the inks, inside the syringe and prior to printing, could also be evaluated as a contributing factor to improved long-range ordering. Resting temperature could also have an impact on cluster size and overall micellar packing.

Irrespective of the original micellar packing, we verified that UV-Vis exposure promoted disorder in the system, observed as broader Bragg peaks and more intense isotropic halos. This effect was more pronounced in fully methacrylated samples, indicating that intra- and inter-micellar chemical bonds may disrupt both the micelle structure and the micellar packing integrity. It can be assumed that a fraction of the micellar packing clusters remains intact after photo-crosslinking, but with reduced size, and it cannot be neglected that an increased number of uncorrelated micelles coexist with these smaller clusters.

Figure 9 shows an illustrative scheme summarizing the nanostructural effects observed during the 3D printing of the photo-crosslinkable micellar inks. The results suggest that initially, the inks at rest in the syringe, consist of large micellar clusters arranged in cubic phases and randomly oriented. With the start of 3D printing, the shearing forces of extrusion cause clusters orientation with the flow, in order to favor planes of longer interplanar distances (slip planes) parallel to the flow direction (Figure 5). These micellar planes also slide over each other, through slip mechanisms, to accommodate the shear stress.

The excessive shear stress can result in slip planes correlation losses, reducing the long-range ordering and increasing the fraction of isotropically distributed micelles. Furthermore, the possibility of micellar disruption during extrusion is not excluded. In agreement with the results of (Rodriguez-Palomo et al., 2021), cluster orientation was better observed with the largest nozzle used (1 mm cylindrical), given that lower shear stress reduces the plane slipping effect.

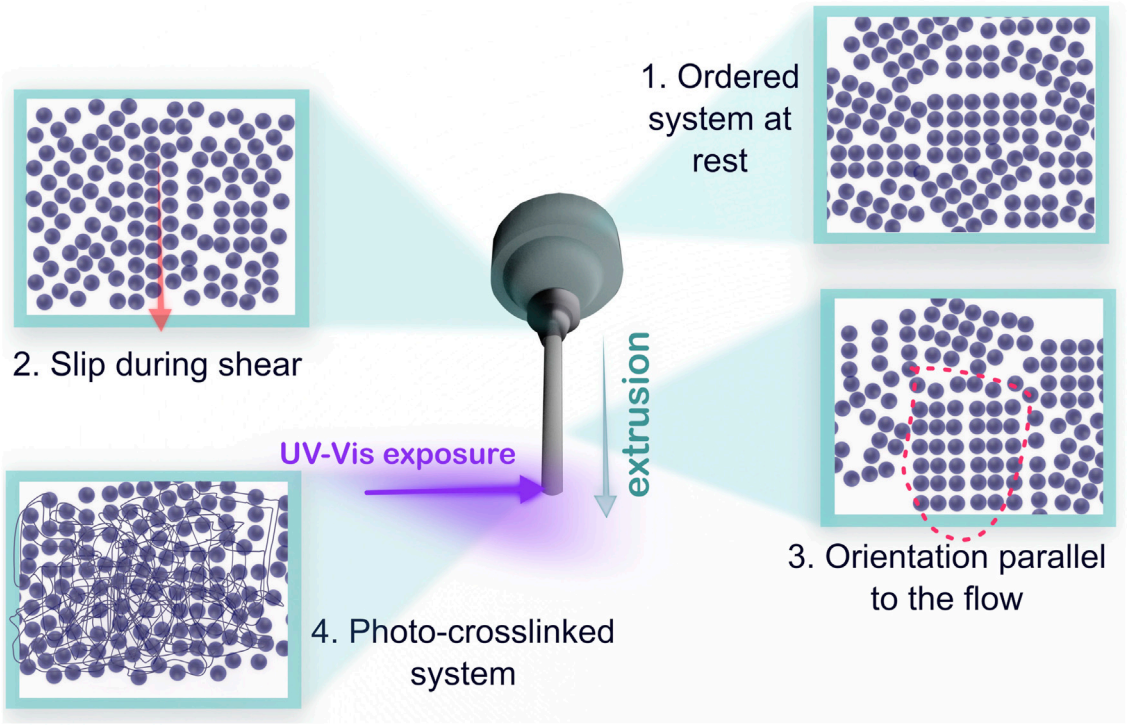

FIGURE 9
Schematic representation of the structural effects observed during extrusion 3D printing and photo-crosslinking. The micelles are represented as rigid spheres. The ordered sequences of these spheres represent clusters with bcc or fcc micellar packing.

After extrusion, the shear stress imposed on the ink is interrupted, but nanostructural disruption is sustained for a small period of time. Afterwards, the system tends to recover both the micellar packing arrangement and the random orientation of clusters, leading to a more isotropic scattering intensity distribution. Therefore, it is likely that nanostructural loss and recovery are kinetically limited by the cooperative movement of the Pluronic chains that compose the clusters, micelles, and unimers. Additionally, it is worth noting that the methacrylate groups at the chain ends reduce the rate of nanostructural recovery of F127-DM inks, as they are bulkier groups than the original hydroxyl groups, and further restrict movement.

Theoretical calculations of molecular volumes for hydroxyl and methacrylate groups reveal that the molecular volume of the terminal methacrylate group (approximately 100 $Å^3$) is five times greater than that of the hydroxyl group (approximately 20 $Å^3$), as illustrated in Supplementary Figure S11A. This difference suggests that the bulkier methacrylate groups are likely to introduce a more substantial steric hindrance, thereby exerting a greater diffusional constraint in the intermicellar space compared to the terminal hydroxyls. Consequently, one may expect a slower micellar dynamics with a delayed nanostructural recovery for the F127-DM, as observed. Furthermore, the larger methacrylate groups are also expected to impact the interpenetration dynamics of micelle crowns during the gelation process, leading to a decreased micellar packing efficiency, in accordance with the SAXS patterns.

Finally, we verified that nanostructural recovery is not hindered by the photo-crosslinking process and, in fact, that these are competitive mechanisms during UV-Vis light exposure. Since photo-crosslinking promotes the formation of inter- and intra-micellar chemical bonds, irreversible effects such as micellar rupture, increased size distribution of micellar clusters, and a decrease in long-range order were found. The final hydrogel after 3D printing/post-printing process shows smaller fraction of preserved cubic phase distributed in clusters with a broad range of sizes.

5 Conclusion

The presence of methacrylate groups at the chain ends of F127 is essential for achieving self-supported constructs, however, it turns F127-DM inks more susceptible to nanostructural disruption during 3D printing. The rate of nanostructural recovery after extrusion is significantly reduced by the methacrylate group addition. Therefore, a compromise must be made to allow sufficient recovery time after printing without filament drying prior to (or during) photo-crosslinking.

The choice of nozzle size and shape as well as the extrusion rate plays a critical role in 3D printing resolution and nanostructural retention. Even though larger nozzles exhibit lower printing resolution, they showed higher micellar packing retention. In contrast, conical nozzles showed significant micellar packing

disruption in comparison with cylindrical nozzles. Finally, higher extrusion rates increase the shear stress that disrupts, preferentially, the fcc phase of the F127-DM micellar packing. Therefore, for F127-DM ink the best printing conditions are large cylindrical nozzles at low extrusion rates.

The photo-crosslinking post-processing is necessary to maintain the shape fidelity and increase the mechanical resistance of the constructs. On the crosslinked filaments, cluster size is reduced, but the micellar packing within the clusters is improved in comparison with the freshly extruded filaments. Partial micellar disruption and a large fraction of isotropically distributed micelles are also consequences of photo-crosslinking.

In conclusion, the *in situ* and *in operando* synchrotron experiments implemented at the CATERETÊ (Sirius - Brazil) and CoSAXS (MAXIV–Sweden) beamlines allowed a systematic study of the printing parameters of Pluronic dimethacrylate inks from a nanostructural perspective. These novel methodologies open up the possibility of investigating further printing conditions, such as printing temperature and drug loading, as well as several other nanostructured inks.

Data availability statement

The raw data supporting the conclusion of this article will be made available by the authors, without undue reservation.

Author contributions

MB: Conceptualization, Data curation, Formal Analysis, Investigation, Validation, Visualization, Writing–original draft, Writing–review and editing. LdS: Conceptualization, Data curation, Formal Analysis, Investigation, Validation, Writing–review and editing. PM-S: Investigation, Methodology, Software, Writing–review and editing. MdO: Conceptualization, Funding acquisition, Project administration, Resources, Writing–review and editing. TP: Data curation, Formal Analysis, Investigation, Methodology, Resources, Writing–review and editing.

Funding

The author(s) declare financial support was received for the research, authorship, and/or publication of this article. This work was supported by the São Paulo Research Foundation (FAPESP) [grant numbers 2022/13352-1 (MB), 2016/02414-5 (MdO) and, 2018/14142-5 (LdS)] and the Swedish Governmental Agency for Innovation Systems under contract 2013-44950-102300094.9 (PM-S).

Acknowledgments

This research used facilities of the Brazilian Synchrotron Light Laboratory (LNLS), part of the Brazilian Center for Research in Energy and Materials (CNPEM), a private non-profit organization under the supervision of the Brazilian Ministry for Science, Technology, and Innovations (MCTI). The CATERETÊ beamline staff is acknowledged for the assistance during the experiments (Proposal 20221941), particularly our local contact Dr. Aline Ribeiro Passos. Research conducted at MAX IV Laboratory (CoSAXS beamline, Proposal 20220874), a Swedish national user facility, is supported by the Swedish Research council under contract 2018-07152, the Swedish Governmental Agency for Innovation Systems under contract 2018-04969, and Formas under contract 2019-02496. We also acknowledge the São Paulo Research Foundation (FAPESP) [grant numbers 2022/13352-1 (MB), 2016/02414-5 (MdO) and, 2018/14142-5 (LdS)] for the funding, and MSc. Anna P. R. de Queiroga, MSc. Daniela A. V. F da Rocha, MSc. Herllan V. de Almeida, and MSc. Hilda C. N. Nogueira for their support during the beamtime at CATERETÊ, and Mr. Bruno de Almeida Piscelli for theoretical calculations of molecular volumes.

Conflict of interest

The authors declare that the research was conducted in the absence of any commercial or financial relationships that could be construed as a potential conflict of interest.

The author(s) declared that they were an editorial board member of Frontiers, at the time of submission. This had no impact on the peer review process and the final decision.

Publisher's note

Supplementary material

The Supplementary Material for this article can be found online at: https://www.frontiersin.org/articles/10.3389/frsfm.2024.1354122/full#supplementary-material

References

Abu Owida, H. (2022). Developments and clinical applications of biomimetic tissue regeneration using 3D bioprinting technique. *Appl. Bionics Biomechanics* 2022, 1–12. doi:10.1155/2022/2260216

Ackerson, B. J., and Clark, N. A. (1984). Shear-induced partial translational ordering of a colloidal solid. *Phys. Rev. A* 906, 906–918. doi:10.1103/PhysRevA.30.906

Akash, M. S. H., and Rehman, K. (2015). Recent progress in biomedical applications of Pluronic (PF127): pharmaceutical perspectives. *J. Control. Release* 209, 120–138. doi:10.1016/j.jconrel.2015.04.032

Bashiri, Z., Rajabi Fomeshi, M., Ghasemi Hamidabadi, H., Jafari, D., Alizadeh, S., Nazm Bojnordi, M., et al. (2023). 3D-printed placental-derived bioinks for skin tissue

regeneration with improved angiogenesis and wound healing properties. *Mater. Today Bio* 20, 100666. doi:10.1016/j.mtbio.2023.100666

Bates, F. S., Koppi, K. A., Tirrell, M., Almdal, K., and Mortensen, K. (1994). Influence of shear on the hexagonal-to-disorder transition in a diblock copolymer melt. *Macromolecules* 27, 5934–5936. doi:10.1021/ma00098a060

Bom, S., Ribeiro, R., Ribeiro, H. M., Santos, C., and Marto, J. (2022). On the progress of hydrogel-based 3D printing: correlating rheological properties with printing behaviour. *Int. J. Pharm.* 615, 121506. doi:10.1016/j.ijpharm.2022.121506

Eiser, E., Molino, F., Porte, G., and Pithon, X. (2000). Flow in micellar cubic crystals. *Rheol. Acta* 39, 201–208. doi:10.1007/s003970000083

GhavamiNejad, A., Ashammakhi, N., Wu, X. Y., and Khademhosseini, A. (2020). Crosslinking strategies for 3D bioprinting of polymeric hydrogels. *Small* 16, 2002931. doi:10.1002/smll.202002931

Gioffredi, E., Boffito, M., Calzone, S., Giannitelli, S. M., Rainer, A., Trombetta, M., et al. (2016). Pluronic F127 hydrogel characterization and biofabrication in cellularized constructs for tissue engineering applications. *Procedia Cirp* 49, 125–132. doi:10.1016/j.procir.2015.11.001

Highley, C. B., Rodell, C. B., and Burdick, J. A. (2015). Direct 3D printing of shear-thinning hydrogels into self-healing hydrogels. *Adv. Mater.* 27 (34), 5075–5079. doi:10.1002/adma.201501234

Jang, H. S., Kim, T. H., Do, C., Lee, M. J., and Choi, S. M. (2013). Single-walled carbon nanotube induced re-entrant hexagonal phases in a Pluronic block copolymer system. *Soft Matter* 9, 3050–3056. doi:10.1039/c3sm27589b

Jiang, Y., Zhou, J., Feng, C., Shi, H., Zhao, G., and Bian, Y. (2020). Rheological behavior, 3D printability and the formation of scaffolds with cellulose nanocrystals/gelatin hydrogels. *J. Mater. Sci.* 55, 15709–15725. doi:10.1007/s10853-020-05128-x

Lin-Gibson, S., Bencherif, S., Cooper, J. A., Wetzel, S. J., Antonucci, J. M., Vogel, B. M., et al. (2004). Synthesis and characterization of PEG dimethacrylates and their hydrogels. *Biomacromolecules* 5, 1280–1287. doi:10.1021/bm0498777

Mcconnell, G. A., Lin, M. Y., and Gast, A. P. (1995). Long range order in polymeric micelles under steady shear. *Macromolecules* 28, 6754–6764. doi:10.1021/ma00124a009

Meneau, F., Passos, A. R., Garcia, P. R. A. F., Vinaches, P., Manoel, L., Kalile, T., et al. (2021). Caterete: the coherent X-ray scattering beamline at the fourth-generation synchrotron facility SIRIUS. *Acta Crystallogr.* 77, C283. doi:10.1107/S0108767321093995

Mortensen, K. (2004). Three-dimensional crystallographic determination of the body-centered-cubic morphologies of shear-aligned block copolymer systems. *J. Polym. Sci. Part B Polym. Phys.* 42, 3095–3101. doi:10.1002/polb.20166

Mortensen, K., Almdal, K., Bates, F., Koppi, K., Tirrell, M., and Nord, B. (1995). Shear devices for *in situ* structural studies of block-copolymer melts and solutions. *Phys. B Condens. Matter* 213-214, 682–684. doi:10.1016/0921-4526(95)00248-8

Mortensen, K., Batsberg, W., and Hvidt, S. (2008). Effects of PEO– PPO diblock impurities on the cubic structure of aqueous PEO– PPO– PEO pluronics micelles: fcc and bcc ordered structures in F127. *Macromolecules* 41, 1720–1727. doi:10.1021/ma702269c

Mortensen, K., and Pedersen, J. S. (1993). Structural study on the micelle formation of polyethylene oxide-Poly(propylene oxide)-Poly(ethylene oxide) triblock copolymer in aqueous solution. *Macromolecules* 26, 805–812. doi:10.1021/ma00056a035

Müller, M., Becher, J., Schnabelrauch, M., and Zenobi-Wong, M. (2015). Nanostructured Pluronic hydrogels as bioinks for 3D bioprinting. *Biofabrication* 7, 035006. doi:10.1088/1758-5090/7/3/035006

Niu, G., Du, F., Song, L., Zhang, H., Yang, J., Cao, H., et al. (2009). Synthesis and characterization of reactive poloxamer 407s for biomedical applications. *J. Control. release* 138, 49–56. doi:10.1016/j.jconrel.2009.04.026

Picheth, G. F., Marini, T. C., Taladriz-Blanco, P., Shimamoto, G. G., dos Santos, G. J. V. P., Meneau, F., et al. (2019). Influence of Pluronic F127 microenvironments on the photochemical nitric oxide release from S-nitrosoglutathione. *J. Colloid Interface Sci.* 544, 217–229. doi:10.1016/j.jcis.2019.02.087

Plivelic, T. S., Terry, A. E., Appio, R., Theodor, K., and Klementiev, K. (2019). X-ray tracing, design and construction of an optimized optics scheme for CoSAXS, the small angle x-ray scattering beamline at MAX IV laboratory. *AIP Conf. Proc.* 2054. doi:10.1063/1.5084576

Pozzo, D. C., and Walker, L. M. (2007). Shear orientation of nanoparticle arrays templated in a thermoreversible block copolymer micellar crystal. *Macromolecules* 40, 5801–5811. doi:10.1021/ma0700173

Puza, F., and Lienkamp, K. (2022). 3D printing of polymer hydrogels—from basic techniques to programmable actuation. *Adv. Funct. Mater.* 32, 2205345. doi:10.1002/adfm.202205345

Rodriguez-Palomo, A., Lutz-Bueno, V., Guizar-Sicairos, M., Kádár, R., Andersson, M., and Liebi, M. (2021). Nanostructure and anisotropy of 3D printed lyotropic liquid crystals studied by scattering and birefringence imaging. *Addit. Manuf.* 47, 102289. doi:10.1016/j.addma.2021.102289

Schwab, A., Levato, R., D'Este, M., Piluso, S., Eglin, D., and Malda, J. (2020). Printability and shape fidelity of bioinks in 3D bioprinting. *Chem. Rev.* 120, 11028–11055. doi:10.1021/acs.chemrev.0c00084

Seoane-Viaño, I., Januskaite, P., Alvarez-Lorenzo, C., Basit, A. W., and Goyanes, A. (2021). Semi-solid extrusion 3D printing in drug delivery and biomedicine: Personalised solutions for healthcare challenges. *J. Control. Release* 332, 367–389. doi:10.1016/j.jconrel.2021.02.027

Shriky, B., Kelly, A., Isreb, M., Babenko, M., Mahmoudi, N., Rogers, S., et al. (2020). Pluronic F127 thermosensitive injectable smart hydrogels for controlled drug delivery system development. *J. Colloid Interface Sci.* 565, 119–130. doi:10.1016/j.jcis.2019.12.096

Smith, P. T., Basu, A., Saha, A., and Nelson, A. (2018). Chemical modification and printability of shear-thinning hydrogel inks for direct-write 3D printing. *Polymer* 152, 42–50. doi:10.1016/j.polymer.2018.01.070

Song, S. J., Choi, J., Park, Y. D., Lee, J. J., Hong, S. Y., and Sun, K. (2010). A three-dimensional bioprinting system for use with a hydrogel-based biomaterial and printing parameter characterization. *Artif. Organs* 34, 1044–1048. doi:10.1111/j.1525-1594.2010.01143.x

Wanka, G., Hoffmann, H., and Ulbricht, W. (1994). Phase diagrams and aggregation behavior of poly(oxyethylene)-poly(oxypropylene)-poly(oxyethylene) triblock copolymers in aqueous solutions. *Macromolecules* 27 (15), 4145–4159. doi:10.1021/ma00093a016

Wu, C., Liu, T., and Chu, B. (1998). A new separation medium for DNA capillary electrophoresis: self-assembly behavior of Pluronic polyol E99P69E99 in 1X TBE buffer. *J. non-crystalline solids* 235-237, 605–611. doi:10.1016/S0022-3093(98)00570-5

Yu, Y., Cheng, Y., Tong, J., Zhang, L., Wei, Y., and Tian, M. (2021). Recent advances in thermo-sensitive hydrogels for drug delivery. *J. Mater. Chem. B. R. Soc. Chem.* 9, 2979–2992. doi:10.1039/d0tb02877k

Zarrintaj, P., Ramsey, J. D., Samadi, A., Atoufi, Z., Yazdi, M. K., Ganjali, M. R., et al. (2020). Poloxamer: a versatile tri-block copolymer for biomedical applications. *Acta Biomater. Acta Mater. Inc.* 110, 37–67. doi:10.1016/j.actbio.2020.04.028